ADVANCED FUNCTIONAL MATERIALS
www.afm-journal.de

Stable Li Metal Anode Enabled by Simultaneous Regulation of Electrolyte Solvation Chemistry and The Solid Electrolyte Interphase

Hongyu Zhang, Xiaowei Chen, Guanglin Xia, and Xuebin Yu**

The application of Li metal batteries is hindered by the uncontrollable growth of Li dendrites due to the lack of control over Li ion transfer and the formation of solid electrolyte interphase (SEI). Herein, polypropylene (PP) separator modified with acyclic polyaminoborane (PAB, $(NH_2\text{-}BH_2)_n$) and polyiminoborane (PIB, $(NH{=}BH)_n$) is developed to regulate electrolyte solvation chemistry and simultaneously facilitate the construction of robust SEI. The mediating effect of PAB and PIB promotes favorable formation of $(O)_2{-}Li^+{-}N$ to weaken the Li bonds between Li ion and solvent in the electrolyte, which homogenizes Li ion diffusion and reduces the desolvation barrier of Li ions. Additionally, the increase of anions content in the solvation sheath and the reaction between Li metal and PAB and PIB can induce the formation of $[LiNBH]_n$-enhanced SEI enriched with LiF and Li_3N that have Li ion conductivity and mechanical strength to tolerate the volume change of Li metal anode. Therefore, the symmetric cell exhibits a cycling lifetime of over 4000 h.

1. Introduction

The development of Li-based secondary batteries with high energy density is a critical research focus due to the ever-growing demand of electronic applications.[1] Li metal with high theoretical specific capacity (3860 mA h g^{-1}) and low electrochemical potential (−3.04 V versus standard hydrogen electrode) has been widely regarded as the "Holy Grail" anode of Li-based secondary batteries.[2] Nevertheless, the practical application of Li metal anodes is considerably hindered by their short life and safety risks due to the pierce of separator by thus-formed Li dendrites upon cycling charge and discharge process.[3] The uncontrollable growth of Li dendrites could be triggered by the self-enhanced preferential deposition of Li on naturally formed tips and protrusions.[3a,4] On the other hand, the high chemical reactivity of Li metal leads to the spontaneous formation of solid electrolyte interphase (SEI) on the surface of Li metal and the heterogenous nature of SEI film results in the nonuniform Li ion flux on Li metal, which will accelerate the uneven deposition of Li and finally the formation of Li dendrites.[5] Moreover, due to the infinite volume change of Li metal, this vulnerable SEI film is prone to fracture during Li stripping/plating process, resulting in the continuous exposure of fresh Li underneath, which could further aggravate the formation of Li dendrites at the exposed site.[5a,6] In addition, the continuous repairing of SEI film would lead to low coulombic efficiency, depletion of electrolyte, and hence rapid degradation of capacity.[7]

Accordingly, considerable efforts have been devoted to suppressing the uneven growth of Li dendrites and improving the cycling stability of Li metal anodes. Among them, optimizing the composition of electrolyte with additives is able to stabilize Li metal anodes via the formation of a stable passivation layer.[8] In addition, the stability of Li metal anodes could also be improved via direct modification of Li metal anode, such as building artificial protective layer[6,9] and designing conductive 3D frameworks.[10] Unfortunately, the cycling stability of Li metal anode is still unsatisfactory, since, in addition to Li metal anode, the separator, as an important part of battery, also plays a critical role in determining the cell's electrochemical performance. When Li ions in the electrolyte pass through the separator, they are mostly trapped in the pores of separators, which leads to the aggregation of Li^+ near the surface of these separator pores and thereby the lack of Li^+ on the other side facing the ionically insulated separator skeleton.[11] The anisotropic distribution of Li^+ would inevitably induce heterogeneous nucleation and plating of Li and eventually the uncontrollable growth of Li dendrites. Moreover, according to "sand's time" theory, the rapid consumption of Li^+ at the vicinity of electrode creates a space-charge region, which could result in the rapid growth of dendrites on the surface of Li metal anode. Therefore, the modification of separators is believed to be a prerequisite for the stabilization of Li metal anodes. It has been experimentally demonstrated that the modification of separator with lithiophilic sites and even Li ion conductor with polar functional groups that could redistribute and homogenize the Li ion flux effectively suppresses the growth of Li dendrites.[11,12]

H. Zhang, G. Xia, X. Yu
Department of Materials Science
Fudan University
Shanghai 200433, China
E-mail: xiaguanglin@fudan.edu.cn; yuxuebin@fudan.edu.cn
X. Chen
School of Science
Jimei University
Xiamen 361021, China

The ORCID identification number(s) for the author(s) of this article can be found under https://doi.org/10.1002/adfm.202301976

DOI: 10.1002/adfm.202301976

However, the introduction of these lithiophilic sites and Li ion conductors with heavy weight not only tremendously reduces the total energy density of the battery, but also could inevitably block partial pores of separators and hence delay the Li ion diffusion kinetics.[13] In addition, the intrinsic issues of the growth of Li dendrites on the surface of Li metal anodes could not be effectively solved by the mere modification of separators. Hence, the development of a facile strategy to modify both the separator and Li metal simultaneously is highly desirable and, indeed, imperative for realizing long-term cycling stability of Li metal anodes.

Herein, we report the modification of commercial polypropylene (PP) separator with BN-based chains induced by the dehydrogenation of ammonia borane (NH_3BH_3, AB) that is uniformly infiltrated through a facile solution-immersion method. The presence of BN-based layer effectively reduces the dissociation energy of Li ions from the electrolyte via the building of $(O)_2$–Li^+–N rather than stable O–Li^+–O, which effectively weakens the Li bonds between Li ions and solvent, leading to the improved diffusion kinetics of Li ions in the electrolyte and the promoted desolvation process of Li ions toward homogeneous Li deposition. Furthermore, the introduction of BN-based layer could tune the solvation sheath with the formation anion-rich solvation structure to induce the favorable formation of anion-derived SEI enriched with LiF and Li_3N, which leads to the enhanced Li ion conductivity of thus-formed SEI layers. In addition, partial BN-based layer could react with Li metal to form $[LiNBH]_n$ polymer-like chains inside of thus-formed SEI layers and hence facilitate the formation of $[LiNBH]_n$-enhanced SEI, which could not only increase the toughness of SEI to tolerate the volume variation during Li stripping/plating, but also further facilitate the Li ion transfer due to its high ionic conductivity. In addition, the polar structure like Li-N and B-N bonds in $[LiNBH]_n$ could again direct a uniform Li ion flux at the interphase of Li metal and electrolyte, leading to uniform deposition of Li. As a result, when using BN-based layer modified separator, the symmetric cell exhibits a long life of over 4000 h at 1 mA cm^{-2} and 1 mA h cm^{-2}. More impressively, Li//$LiFePO_4$ (LFP; 12 mg cm^{-2}) full cell exhibits favorable cycling stability of over 500 cycles at 1 C and a reversible capacity of over 800 mA h g^{-1} for Li-S full cell after 300 cycles at 1 C could be achieved.

2. Results and discussion

As schematically illustrated in **Figure 1**a, the modification of PP separator is facile realized by the infiltration of AB via a solution-immersion method, followed by thermally driven hydrogen desorption process of AB. According to the density functional theory (DFT) results (Figure S1, Supporting Information), the binding energy between PP separator and AB is calculated to be −0.41 eV, much lower than that between AB molecule (−0.28 eV). This result indicates the favorable adsorption of AB on PP separator via van der Waals force, which would facilitate the uniform distribution of AB on PP separator, rather than the formation of AB clusters. The mass loading of the as-obtained BN-based layer is only 0.08 mg cm^{-2} (Figure S2, Supporting Information) and hence it has negligible effect on the energy density of the battery. After thermal treatment at 120 °C for hydrogen desorption (Figure S3, Supporting Information), the characteristic peaks of [N-BH_3] of AB at −23.12 and −27.79 ppm in solid-state ^{11}B nuclear magnetic resonance (NMR) spectra (Figure 1b) almost disappear with the appearance of new peaks located at 5~30 ppm and −20~−5 ppm. The peaks at −8.40, −15.88, and −24.78 ppm could be indexed to tetrahedrally coordinated B species (B^{IV}) (i.e., $[N_3BH]_n$, $[N_2BH_2]_n$, and $[NBH_3]_n$, respectively),[14] while the peaks at 21.42 and 9.69 ppm could be attributed to trigonally coordinated B species (B^{III}) from the further dehydrogenation of B^{IV}-based composite (*i.e.*, $[N_2BH]$ and $[BN_3]$).[14,15] In addition, fourier-transform infrared (FTIR) spectra of pure AB and BN@PP at 120 °C (Figure 1c) illustrates the significant weakening of B–H and N–H bonds after thermal treatment, accompanied with the increase intensity of B–N peaks, which demonstrates the intramolecular combination of N–H and B–H via in situ polymerization.[16] These results confirm the formation of acyclic polyaminoborane (PAB, $(NH_2\text{-}BH_2)_n$) and polyiminoborane (PIB, $(NH{=}BH)_n$).[16a,17] from the dehydrogenation of AB according to equation (1) and (2):

$$r NH_3BH_3 \rightarrow \left(NH_2 - BH_2\right)_n + H_2 \quad (1)$$

$$\left(NH_2 - BH_2\right)_n \rightarrow (NH = BH)_n + H_2 \quad (2)$$

X-ray photoelectron spectroscopy (XPS) results confirm the existence of N–B (399.0 eV) and N–H (401.1 eV) bonds in N 1s XPS spectrum (Figure 1d) and the observation of B–H (190.7 eV) and B–N (192.9 eV) bonds in B 1s XPS spectrum (Figure 1e), which provides additional evidence to the successful loading of BN-based layer on PP separator. Moreover, the depth profiles of XPS via Ar ion etching demonstrate that the thickness of BN-based layer coated on PP separator is less than 400 nm (Figure S4, Supporting Information), which corresponds well with the ultralow mass loading of BN-based layer on PP separator. After the loading of BN-based layer on PP separator, the as-obtained BN@PP also shows a comparable porous structure (Figure 1f) with bare PP separator (Figure S5, Supporting Information) without the observation of any particles that could block pores in separator, indicating the homogeneous distribution of BN-based layer on PP separator. The corresponding element mapping of BN@PP illustrates that B and N are uniformly distributed on the separator (Figure 1g), which further proves that BN containing species (PAB and PIB) are homogeneously coated on PP separator owing to the favorable adsorption between PP separator and AB. Owing to the rigid $(NH{=}BH)_n$ species in BN-based layer on PP separator, BN@PP separator exhibits a higher Young's modulus (1408 MPa) than that of pristine PP separator (997 MPa) (Figure S6, Supporting Information), which could reduce the risk of the penetration of separator by Li dendrites.

To evaluate the effect of BN-based layers in tuning Li ion transport behavior through the PP separator, the Li ion transference number and Li ion conductivity of BN@PP are first investigated based on the combination of chronoamperometry and electrochemical impedance spectroscopy (EIS) results of symmetric cells. Since the skeleton of bare PP separator is not ionically conductive and the ion conductivity of separator is mainly contributed to the electrolyte transport through the pores of the separator, the calculated Li ion transference number (**Figure 2**a,b) of bare PP is only 0.31, while this value reaches 0.53 for BN@PP, suggesting the suppressed anion migration and the promoted Li

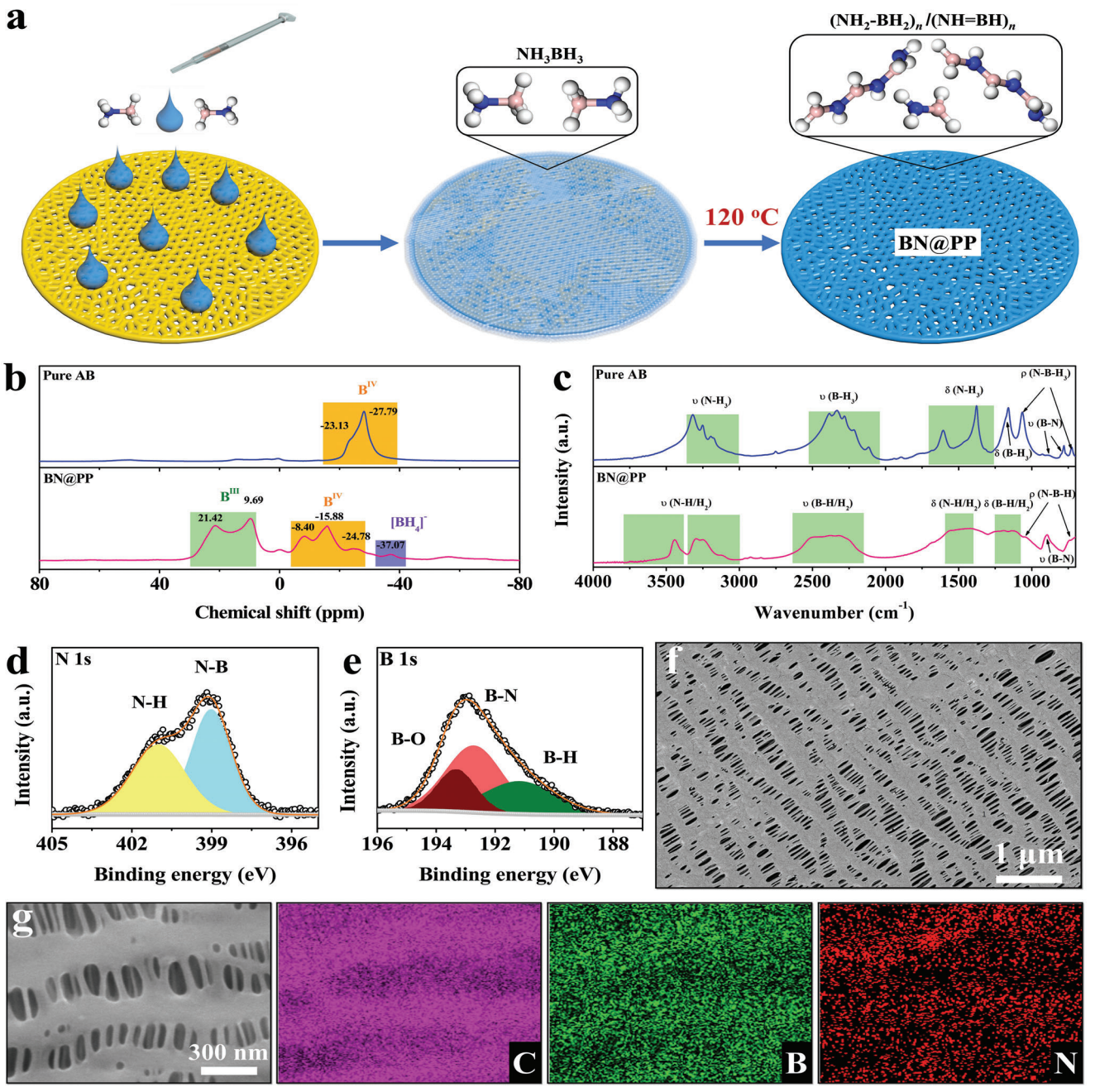

Figure 1. a) Schematic illustration of the fabrication of BN@PP separator. b) Solid state ^{11}B NMR spectra and c) FTIR spectra of pure AB and BN@PP separator. High-resolution d) N 1s and e) B 1s XPS spectra, and f,g) SEM images and corresponding elemental mapping of BN@PP separator.

ion diffusion induced by the presence of BN-based layers with high polarity. Moreover, the Li ion conductivity (Figure 2c) of BN@PP is calculated to be 2.52 mS cm^{-1}, which is also much higher than that of bare PP (1.59 mS cm^{-1}) according to the Nyquist plots of stainless steel (SS) symmetric cell. These results indicate that BN-based layer with large polarity uniformly coated on separator could effectively regulate and facilitate the Li ion transport in the electrolyte, which contributes to inhibiting the growth of Li dendrites. To understand the mechanism behind the improvement of the Li ion conduction of BN@PP, molecule dynamics simulations were performed. According to the results of the snapshots of the electrolyte structure with PP modified with $(NH_2–BH_2)_n$ and $(NH=BH)_n$ (Figure 2d), the radial distribution functions and corresponding coordinated number (CN) are further calculated. Although a slight increase of the CN of 1,3-dioxolane (DOL) and bis(trifluoromethane)sulfonimide ($TFSI^-$) around Li^+ could be observed for PP modified with BN-based layers (Figure 2e; Figure S7, Supporting Information), the CN of dimethoxyethane (DME) that exhibits stronger Li bonds with Li^+ than DOL decreases in the first solvation sheath (Figure 2f).

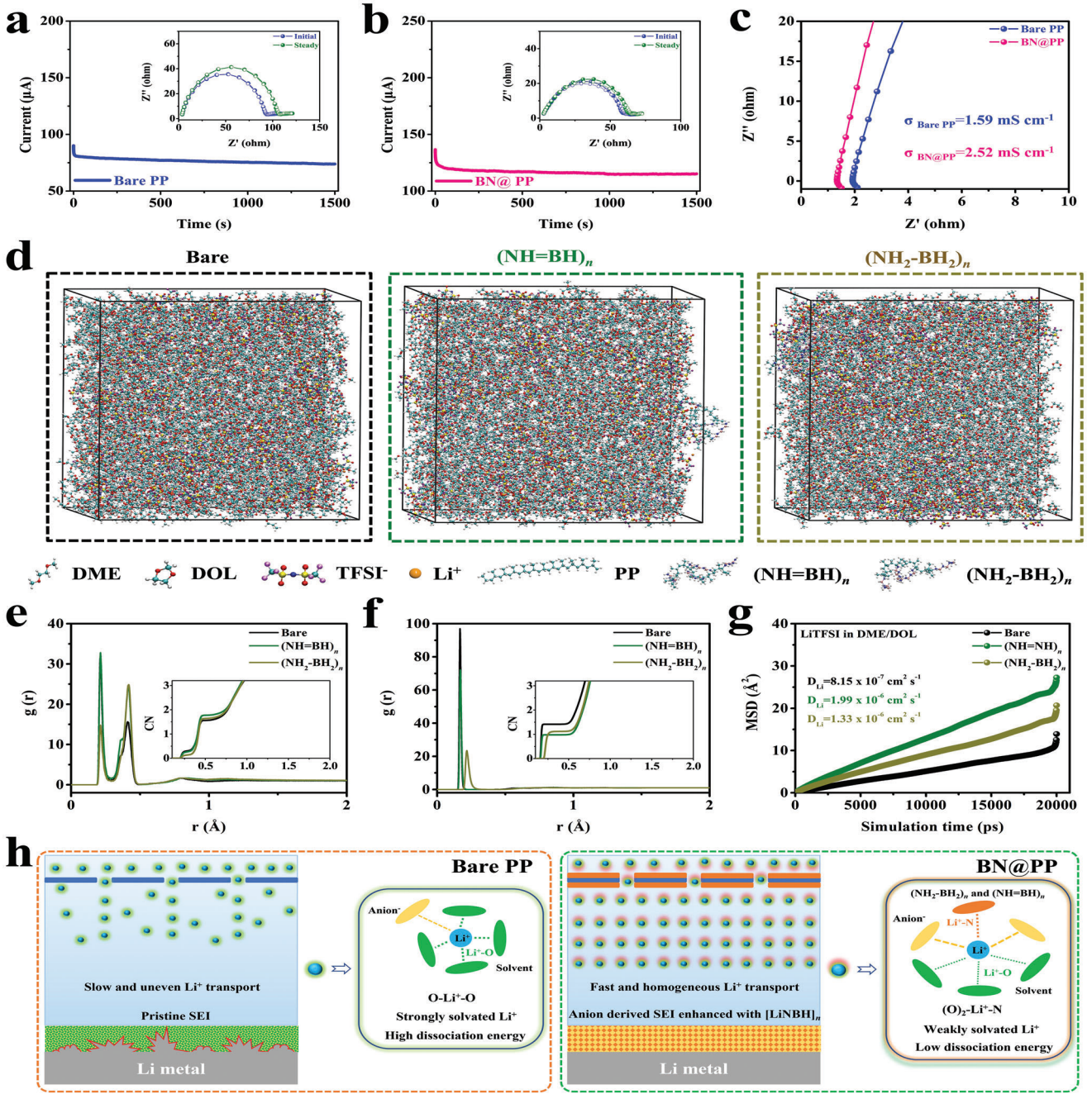

Figure 2. Variation of current with time and EIS tests before and after the polarization of symmetric cells with a) bare PP and b) BN@PP separator. c) Impedance plots of bare PP and BN@PP separator with calculated Li conductivity. d) Snapshots of the simulation system for ether-based electrolyte with bare PP and BN@PP separator. e,f) Radial distribution function g (r) and corresponding coordination number (CN) obtained from MD simulation for Li-TFSI(F) and Li-DME(O), respectively, and g) Mean squared displacements (MSD) of Li^+ in ether-based electrolyte with bare PP and BN@PP separator. h) Schematic illustration for the diffusion and solvation structure of Li ion and the SEI evolution on Li metal when using bare PP and BN@PP separator.

This result demonstrates that the homogeneous decoration of BN-based layers on the surface of PP separator could effectively tune the solvation structure of Li^+ in the electrolyte. To gain more insight into the decrease of DME in the solvation sheath, DFT calculations are performed on a simple Li^+ solvation configuration composed of one Li^+ coordinated with two DME molecular (Figure S8, Supporting Information). Due to the high electronegativity of O atom in DME, Li^+ prefers to strongly coordinate with O atom of DME to form stable Li bonds (O–Li^+–O).[18] Hence, the dissociation energy for $Li^+(DME)_2$ to Li^+(DME) and one DME molecular which indicates the breaking of one of the stable Li bonds (O–Li^+–O) is calculated to be as high as 1.51 eV.

In strong contrast, when $(NH_2\text{-}BH_2)_n$ and $(NH{=}BH)_n$ are introduced into this Li^+ solvation configuration, the corresponding dissociation energy is significantly reduced to 1.31 and 1.09 eV, respectively. The reduced dissociation energy in BN@PP system demonstrates that the strong Li bonds between Li^+ and O atom in DME are significantly weakened due to the mediating effect of N atom in BN-based layers, which promotes the formation of $(O)_2$–Li^+–N rather than stable O–Li^+–O. The introduction of newly-formed Li bonds between Li^+ and N atom in $(NH_2\text{-}BH_2)_n$ and $(NH{=}BH)_n$ effectively weakens the Li bonds between Li^+ and O atom of DME and hence is responsible for the decrease of DME content in the solvation sheath, leading to the promoted desolvation process of Li ions and homogeneous Li deposition.

More interestingly, the $TFSI^-$ content in the first solvation sheath of Li^+ increase due to the weakening of Li bonds between Li^+ and DME and the strengthening of Li bonds between Li^+ and $TFSI^-$ by the presence of BN-based layers on PP. This could reduce the electron acquiring and decomposition of solvent while promote the decomposition of $TFSI^-$ upon cycling Li plating and stripping process, resulting in the formation of anion-derived SEI. As a result, XPS results of cycled Li metal anode using BN@PP as the separator reveal that the content of LiF, which is mainly formed from the decomposition of $TFSI^-$, reaches 21.7%, much higher than that using bare PP as the separator (Figure S9, Supporting Information). Furthermore, the content of Li_3N on cycled Li with BN@PP separator is also much higher than that with bare PP, indicating that the decomposition of $TFSI^-$ also contributes to the formation of Li_3N in SEI. These results directly demonstrate the promoted decomposition of $TFSI^-$ due to its increased content in the first solvation sheath of Li induced by the presence of BN-based layers on PP separator. Although bulk LiF shows a poor Li ion conductivity of 10^{-31} S cm^{-1}, nanocrystal LiF and the possible formation of LiH_xF_{1-x} in SEI favor Li ion transport, and LiF could provide a high ionic conductivity when interfacing with other ingredients at nanoscale due to the low surface diffusion barrier of Li ion.[19] Moreover, electrochemically stable LiF is a good electronic insulator, which could effectively prevent the electron tunneling at the interface of electrode/electrolyte, thus protecting Li metal anode from side reactions with electrolyte. In addition, the low Li ion diffusion barrier and the high surface energy of LiF could promote the uniform and lateral growth of Li under LiF-rich SEI, and improve the cycling performance of Li metal anode.[9d,20] On the other hand, Li_3N has a high Li ion conductivity of $10^{-3}\approx10^{-4}$ S cm^{-1} at room temperature and low electrical conductivity, which could induce higher Li ion concentration beneath the SEI, thus regulating spherical Li deposition, and prevent the growth of dendritic Li.[21] Besides, Li_3N has unique thermodynamic stability against Li metal and high Young's modulus and hence, Li_3N-rich SEI could protect Li metal anode from parasitic reactions and enhance the reversible Li plating/stripping behavior.[22] Therefore, the formation of LiF and Li_3N is widely considered to passivate Li metal surface to reduce side reaction with electrolyte, improve Li^+ diffusion kinetics through SEI, and suppress the formation of Li dendrites,[23] which is capable of effectively improving the cycling stability of Li metal anodes. In addition, according to calculated Li^+ mean squared displacements (MSD) for these electrolytes (Figure 2g), the slopes of BN@PP are steeper than that with bare PP, which provides direct evidence to the faster diffusion of Li^+ through PP separator under the guidance of BN-based layers. It could be attributed to the decrease of DME content in solvation sheath induced by the weakened Li bonds between DME and Li^+, resulting from the introduction of Li bonds between Li^+ and N atoms in BN-based layer in O–Li^+–O to form $(O)_2$–Li^+–N, which effectively reduces the restriction of Li^+ by DME and simultaneously boost Li^+ transfer kinetics in the electrolyte. To verify the universal application of BN@PP, molecule dynamics simulations were also conducted in the commercial electrolyte with $LiPF_6$ solved in ethyl carbonate (EC)/diethyl carbonate (DEC) (Figure S10, Supporting Information). Similar to the results in lithium bis(trifluoromethane)sulfonimide (LiTFSI) in DOL/DME system, the CN of EC and PF_6^- coordinated with Li^+ shows a slight increase when using BN@PP as the separator, while the CN of DEC that exhibits stronger Li bonds with Li^+ decreases in the first solvation sheath. Furthermore, the calculated D_{Li} using BN@PP as the separator is also much higher than that of bare PP (Figure S10g, Supporting Information). These results demonstrate that the homogeneous modification of BN-based layers on PP separator could efficiently tune the solvation sheath of Li^+ by regulating the intensity of Li bonds between Li^+ and solvent/anion, and thus induce fast Li^+ transfer in both ether-based and carbonate electrolyte. It could be concluded that, BN-based layer composed of $(NH_2{-}BH_2)_n$ (PAB) and $(NH{=}BH)_n$ (PIB) species could weaken the Li bonds between Li^+ and solvent to promote the uniform diffusion of Li ion in the electrolyte, reduce the desolvation barrier of Li ion, and facilitate the formation of anion derived SEI enriched with LiF and Li_3N, which effectively contributes to alleviating the formation of Li dendrites. (Figure 2h)

To investigate the role of PP separator modified with BN-based layers in stabilizing Li metal anodes, symmetric cells assembled with BN@PP separator obtained at various temperature with different loading condition are first fabricated and tested at 1 mA cm^{-2} with an areal capacity of 1 mA h cm^{-2} (Figure S11, Supporting Information). In the terms of bare Li metal anode using pure PP separator, the overpotential increases rapidly after only 300 h, and it reaches near 100 mV after 870 h with large fluctuation owing to the continuous accumulation of SEI and "dead Li" and the depletion of electrolyte. In strong contrast, the cycling stability of symmetric cells could be significantly improved when using BN@PP as the separator, which directly confirms the positive role of BN@PP in promoting the uniform deposition of Li. Among all the prepared samples, BN@PP obtained at 120 °C with solution immersion process for 2 times exhibits the best cycling performance and a low overpotential of 13 mV could be achieved after cycling for 4000 h (**Figure 3**a), which could be attributed to the synergistic effect of favorable loading amount and sufficient polymerization of BN species without blocking or destroying the porous structure of PP separator (Figure S12, Supporting Information). Hence, BN@PP prepared under this condition is adopted for detailed investigation and characterization. Upon increasing the current density to 3 mA cm^{-2} with a fixed areal capacity of 3 mA h cm^{-2}, the cells using BN@PP as the separator could still maintain stable voltage profile for over 1500 h with a low overpotential of 25 mV, while the overpotential of the cell using PP separator is increased to 100 mV after cycling for only 210 h (Figure 3b). Moreover, the Li//Cu half cells with BN@PP separator exhibits a coulombic efficiency of

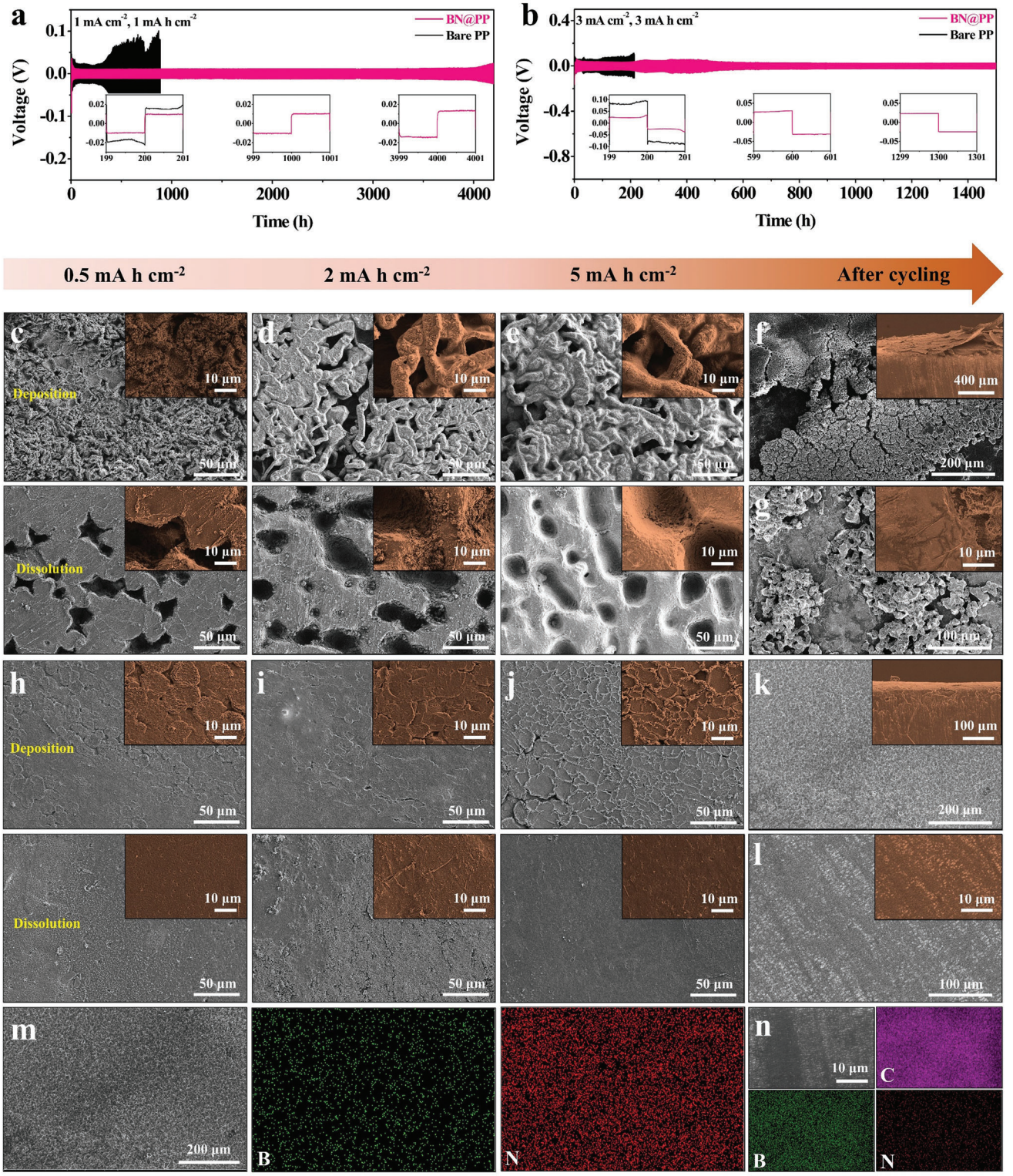

Figure 3. Galvanostatic discharge/charge voltage profile of symmetric cells using bare PP and BN@PP as the separator at a) 1 mA cm^{-2} with a fixed capacity of 1 mA h cm^{-2} and b) 3 mA cm^{-2} with a fixed capacity of 3 mA h cm^{-2}. Top-view SEM images of Li metal after plating and stripping c,h) 0.5, d,i) 2, and e,j) 5 mA h cm^{-2} of Li, respectively, and f,k) Li metal and g,l) separator after 100 cycles in symmetric cells using bare PP and BN@PP as the separator, respectively. SEM images and the corresponding elemental mapping of m) Li metal and n) separator after 100 cycles in symmetric cells with BN@PP separator.

98.8% after 450 cycles at 0.5 mA cm^{-2} with a fixed capacity of 1 mA h cm^{-2}, which is much higher than that with bare PP separator (Figure S13, Supporting Information), indicating the stable reversibility of Li stripping and plating process of Li metal anodes resulting from the modification of PP separator with BN-based layers. With the increase of current density and fixed capacity, the advantage of Li//Cu cell with BN@PP separator is more obvious. The superior cycling stability of both symmetric cells and half cells using BN@PP as the separator than that of PP provides direct evidence to the effective role of BN-based layers in improving the stability of Li metal anodes, which coincides well with the theoretical calculation results.

To further elucidate the mechanism for the enhanced electrochemical performance, XPS is conducted to investigate the surface environment of BN@PP and Li metal anodes after cycling. The N-B peak at 399.2 eV in N 1s XPS spectrum and the B–H and B–N peaks at 189.3 and 191.4 eV in B 1s XPS spectrum, respectively, could be observed for BN@PP close to the surface of Li metal anode after 40 cycles (Figure S14a, Supporting Information), indicating the favorable adsorption of BN-based layer on PP separator without peeling off during repeated Li stripping and plating process, which also contributes to the prolonged lifespan of assembled symmetric cells. On the side of Li metal, the peaks at 399.3 and 396.3 eV in N 1s XPS spectra could be indexed to B–N and Li–NB bonds of $[LiNBH]_n$ (Figure S14b, Supporting Information), which agrees well with B 1s XPS peak at 191.4 eV and Li 1s XPS peak at 53.0 eV, respectively. This result confirms the formation of $[LiNBH]_n$ in the as-formed SEI of Li metal, which could be induced by the side reaction between Li and PAB/PIB in BN-based layer during cycling. The formation of $[LiNBH]_n$, which is uniformly constructed by Li–N and B–N bonds with large polarity based on a molecular level and high Li ion conductivity,[16b] could not only increase the mechanical strength of SEI to promote the stability of Li metal anode, but also facilitate the homogeneous distribution of Li^+ at the interface of Li metal and electrolyte by building Li bonds between Li^+ and N atoms in $[LiNBH]_n$ toward uniform Li stripping and plating of Li metal anodes (Figure 2h). In addition, the characteristic peak of Li_3N and LiF with high intensity could also be clearly detected, which would effectively promote the Li ion conductivity of SEI and simultaneously protect Li metal anode from parasitic reaction. Interestingly, although the content of LiF and Li_3N in the SEI of cycled Li using BN@PP separator is higher than that using pristine PP separator at various cycles (Figure S9, S14, S15, and S16, Supporting Information) due to the formation of anion-derived SEI under the guidance of BN-based layer on PP separator, the content of $[LiNBH]_n$ in the SEI of cycled Li using BN@PP separator increases from 6.6% to 12.7% while the content of LiF and Li_3N decreases from 21.7% and 50.5% to 19.2% and 34.8%, respectively, from 20 to 40 cycles. This could be attributed to the stitching effect of PAB/PIB in BN-based layer that could react with the exposed fresh Li at the cracks toward the formation of $[LiNBH]_n$ and hence repair and strengthen SEI. It is worth noted that the content of LiF, Li_3N, and $[LiNBH]_n$ in the SEI of cycled Li using BN@PP separator shows negligible change from 40 to 100 cycles (Figure S17, Supporting Information), which indicates that the decomposition of electrolyte including LiTFSI and solvents and the formation of $[LiNBH]_n$ at cracks reach equilibrium after 40 cycles. Meanwhile, this also demonstrates that the as-formed $[LiNBH]_n$-enhanced SEI is stable and flexible, which could tolerate the volume change during cycling, and reduced the continuous cracking and repairing of SEI to a large extent. Therefore, the $[LiNBH]_n$-enhanced SEI could suppress the side reaction between Li and $TFSI^-$ and solvents, which avoids the continuous consumption and eventually the depletion of electrolyte, thus leading to improved cycling lifespan. Considering that the content of LiF and Li_3N in the SEI of cycled Li using pristine PP separator from 40 to 100 cycles also shows slight change, it could be concluded that when the components of the SEI becomes stable, the content of LiF and Li_3N in the SEI of cycled Li using BN@PP separator could be promoted from 11.3% and 13.8% to 19.0% and 34.0%, respectively, with the formation of 12.6% of $[LiNBH]_n$ under the guidance of BN-based layer on PP separator.

EIS analysis is subsequently conducted to directly investigate the interfacial charge transfer of the symmetric cells (Figure S18 and Table S1, Supporting Information). The SEI resistance (R_{SEI}) and interfacial charge transfer resistance (R_{ct}) for symmetric cells using BN@PP separator is much lower than that using pristine PP separator before and after cycling. This indicates that the $[LiNBH]_n$-enhanced SEI with higher content of Li_3N and LiF could induce fast Li ion diffusion during Li stripping/deposition, and the charge transfer at the interface between Li metal anode and electrolyte is also improved when using BN@PP as the separator. Furthermore, it is noteworthy that the rapid increase of R_{SEI} could be observed for symmetric cells when using pristine PP separator after 20 cycles, due to the continuous thickening of SEI after repeated cracking and repairing and the accumulation of "dead Li". In strong contrast, symmetric cells using BN@PP separator exhibits a much lower R_{SEI} and no obvious increase of R_{SEI} could be observed upon cycling. This demonstrates that the as-formed SEI containing $[LiNBH]_n$ could withstand structural fracture, which significantly avoids the thickening of SEI and suppresses the formation of "dead Li". More importantly, the increased content of $[LiNBH]_n$ upon cycling could still preserve the excellent Li ion transport behavior in SEI due to the high Li ion conductivity of $[LiNBH]_n$,[16b] although the content of LiF and Li_3N in the as-formed SEI decreases to some degree. In addition, the exchange current density (I_0) in symmetric cells using BN@PP separator is also much higher than that in symmetric cells using pristine PP separator after 20 (Figure S19, Supporting Information), 50 (Figure S20, Supporting Information), and 100 cycles (Figure S21, Supporting Information), which further verifies the enhanced interfacial Li ion migration kinetics owing to the formation of $[LiNBH]_n$ and higher content of Li_3N and LiF in SEI induced by BN@PP separator.

In addition, BN@PP separator is also applied and tested in commercial carbonate-based electrolyte. Symmetric cells using BN@PP separator exhibit stable cycling for 1500 h with low overpotential of 54 mV at 1 mA cm^{-2} with a fixed capacity of 1 mA h cm^{-2} (Figure S22, Supporting Information), and a cycling life of over 600 h could be obtained for symmetric cells using BN@PP separator even at 3 mA cm^{-2} with a fixed capacity of 3 mA h cm^{-2} (Figure S23, Supporting Information), which are much better than that using pristine PP separator. It is worth noted that the electrochemical performance of symmetric cells of Li metals with BN@PP separator is among the best reported Li metal anodes using modified separators (Table S2, Supporting Information). The improved cycling performance

by using BN@PP separator could be attributed to the accelerated Li ion diffusion in the electrolyte and the as-formed $[LiNBH]_n$-enhanced anion-derived SEI, corresponding well with the molecule dynamics simulations results in carbonate electrolyte. To test the availability of BN@PP in other alkali metal batteries, BN@PP was also applied to Na and K metal batteries using ether-based electrolyte. In the symmetric cells of Na metals, a stable cycling life of 1200 and 700 h with low overpotential of 13 and 16 mV could be obtained at 3 mA cm^{-2}, with fixed capacities of 1 mA h cm^{-2} (Figure S24, Supporting Information) and 3 mA h cm^{-2} (Figure S25, Supporting Information), respectively. More impressively, when using BN@PP as the separator of symmetric cells of K metals, a long lifespan of 700 and 500 h at 1 (Figure S26, Supporting Information) and 2 mA cm^{-2} (Figure S27, Supporting Information), respectively, could be achieved with a fixed areal capacity of 1 mA h cm^{-2}, although K metal anode suffers from more serious challenges than Li and Na metal anodes.[24] These results directly demonstrate the effective and universal role of BN@PP separator in regulating the deposition of other alkali metals and promoting their cycling stability of alkali metal batteries.

The role of BN@PP separator in regulating Li plating and stripping performance of Li metal was subsequently investigated using scanning electronic microscopy (SEM). After plating 0.5 mA h cm^{-2} of Li (Figure 3c; Figure S28a, Supporting Information) in a symmetric cell, mossy Li with uneven distribution could be clearly observed on the surface of Li when using pristine PP separator. Upon increasing Li plating capacity to 2 (Figure 3d; Figure S28b, Supporting Information) and 5 mA h cm^{-2} (Figure 3e; Figure S28c, Supporting Information), Li dendrites grow drastically on the surface of Li metal and the surface of Li metal on the opposite side is full of big holes due to the uneven Li stripping process. After 50 cycles (Figure S29, Supporting Information), obvious formation of "dead Li" layer could be observed on the surface of Li with partial "dead Li" layer even peeling off from the electrode. These "dead Li" layers would become thicker and are prone to fall off after Li plating and stripping for 100 and 300 cycles (Figure 3f; Figure S30, Supporting Information). It is worth noting that part of "dead Li" and Li dendrites could also be found on the surface of the PP separator (Figure 3g; Figure S30c, Supporting Information), which increases the risk of the pierce of separator and short circuit. In strong contrast, when using BN@PP as the separator, the plated Li exhibits a sheet-like structure, which gradually grows uniformly and densely upon the proceeding of Li deposition (Figure 3h–j; Figure S31, Supporting Information). The even deposition of Li could be attributed to fast and uniform Li ion transport in electrolyte and SEI, and low desolvation barrier of Li ions with the help of BN-based layer on PP separator. It is worth mentioned that Li deposition with sheet-like structure indirectly confirms the high Li ion diffusion rate in the as-formed SEI layers strengthened by $[LiNBH]_n$,[21a] coinciding well with the molecule dynamics simulations results and XPS results of cycled Li metal using BN@PP separator. Besides, the Li stripping process when using BN@PP separator becomes more moderate and uniform. These findings further demonstrate that BN-based layer on separator could accelerate and homogenize Li ion diffusion in the electrolyte to suppress the formation of Li dendrites, while the as-formed $[LiNBH]_n$-enhanced SEI enriched with Li-N and B-N bonds with large polarity could further promote and guide the uniform plating/stripping of Li. Moreover, after 50 (Figure S32, Supporting Information), 100 cycles (Figure 3k,l), and 300 cycles (Figure S33a–c, Supporting Information), owing to the uniform Li plating/stripping induced by BN-based layer and the as-formed $[LiNBH]_n$-enhanced SEI, the surface of Li metal is relatively smooth and dense, and no obvious "dead Li" or Li dendrites could be observed on the BN@PP separator side. The characteristic XPS peaks indexed to BN-based species and the uniform distribution of B and N element on Li metal (Figure 3m; Figure S9a, S14b, S16, and S34, Supporting Information) and BN@PP separator (Figure 3n; Figure S14a, S35, S36, and S33d, Supporting Information) after cycling, further demonstrates that the in situ formed $[LiNBH]_n$-enhanced SEI on Li metal and BN-based layer on the separator could be well preserved upon cycling, which could consistently regulate and promote the diffusion of Li ion in both SEI and electrolyte, and guide the uniform plating/stripping of Li.

To further evaluate the feasibility of BN@PP under practical conditions, full cells coupled with commercial LFP with a loading of 12 mg cm^{-2} are first assembled and investigated. Rate capability demonstrates that the Li//LFP full cell with BN@PP separator exhibits higher reversible specific capacity than that with bare PP separator at various rates (**Figure 4**a). The improved capacity of Li//LFP full cells with BN@PP separator could be attributed to fast Li ion diffusion kinetics through PP separator and $[LiNBH]_n$-enhanced SEI as verified by the lower polarization in the discharge/charge profiles at various current densities (Figure S37, Supporting Information). In long-term cycling at 1 C (Figure 4b), the full cell assembled with bare PP separator shows a rapid capacity degradation after only 130 cycles and the capacity retention is only 65.7% after 160 cycles. This could be ascribed to the increase of internal resistance and polarization (Figure S38, Supporting Information) and the consumption of Li and electrolyte due to the severe formation of thick SEI and the accumulation of "dead Li" (Figure 4c,d; Figure S39, Supporting Information) on the surface of Li metal anode during repeated Li plating/stripping process. In contrast, Li//LFP full cell with BN@PP separator exhibits a much higher specific capacity of 129 mA h g^{-1} with a capacity retention of 86.7% after 500 cycles, owing to the uniform deposition/stripping of Li and the suppressed formation of thick SEI and "dead Li" under the guidance of BN-based layer on the separator and $[LiNBH]_n$-enhanced SEI (Figure 4e,f; Figure S40, Supporting Information). Moreover, BN@PP separator is also employed in Li// $LiNi_{0.5}Co_{0.2}Mn_{0.3}O_2$ (NCM523; 10 mg cm^{-2}) full cells. Li//NCM523 full cell coupled with BN@PP separator exhibits a specific capacity of 110 mA h g^{-1} with a capacity retention of 71.4% after 300 cycles, which is much better than that of the full cell coupled with bare PP separator (Figure 4g). The enhanced cycling performance by using BN@PP could be also be explained by the lower polarization (Figure S41, Supporting Information) and the more uniform and denser deposition/dissolution of Li upon cycling (Figure S42 and S43, Supporting Information), rather than the severe formation of "dead Li" and thick SEI on cycled Li when using pristine PP as the separator (Figure S44 and S45, Supporting Information). To further investigate the potential application of BN@PP under practical conditions, the electrochemical performance of full cells with a high areal capacity of LFP cathode (5.1 mA h cm^{-2}) is further

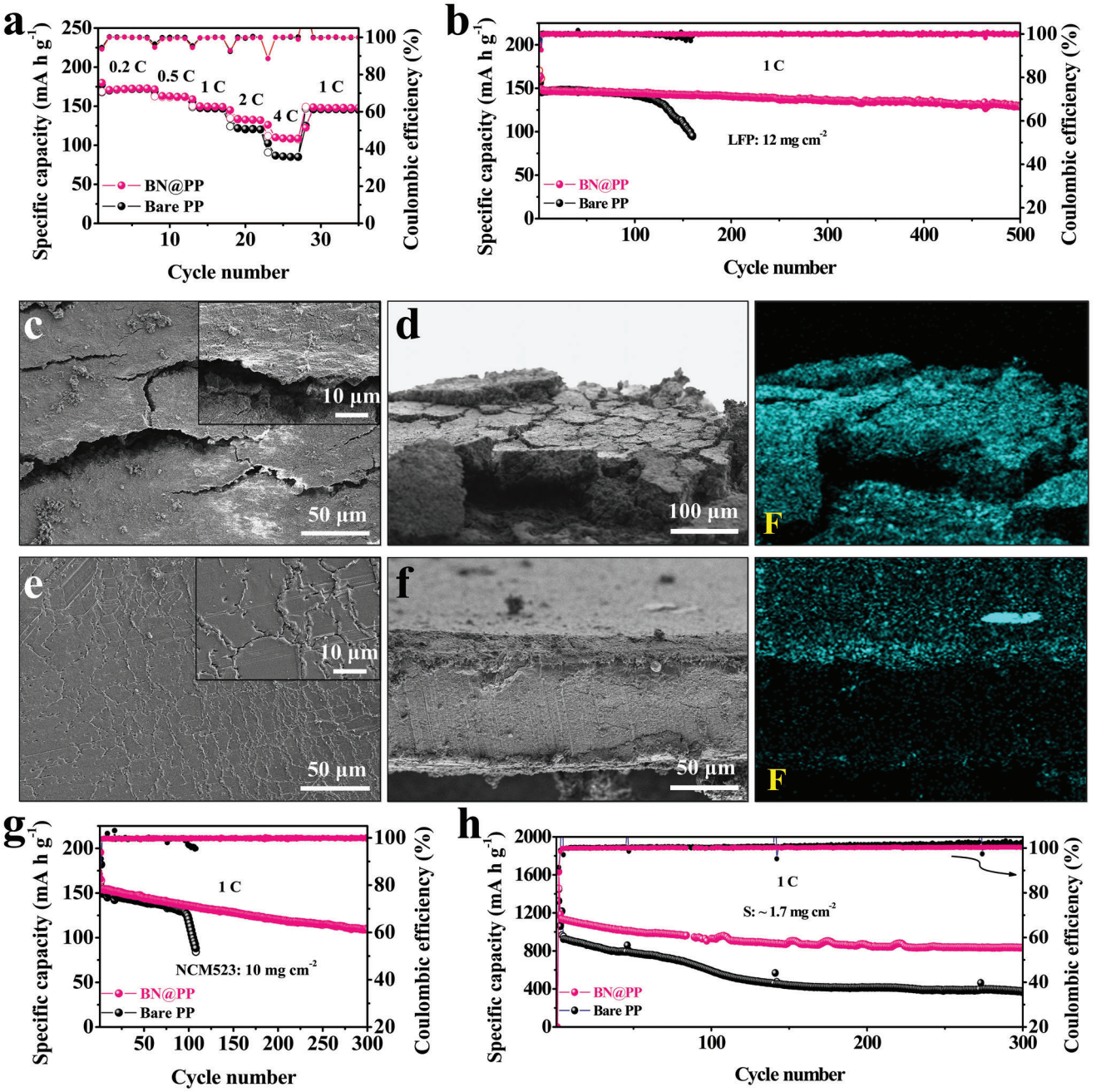

Figure 4. a) Cycling performance and b) the corresponding charge/discharge profiles of Li//LFP full cells with bare PP and BN@PP separator at 1 C (1 C = 170 mA g^{-1}). Top-view and cross-sectional SEM images with the corresponding elemental mapping of Li metal after cycling in Li//LFP full cells with c,d) bare PP and e,f) BN@PP for 40 cycles. g,h) Cycling performance of Li//NCM523 (1 C = 170 mA g^{-1}) and Li//S (1 C = 1650 mA g^{-1}) full cells using bare PP and BN@PP as the separator at 1 C.

investigated. Upon cycling at 0.5 C (Figure S46, Supporting Information), Li//LFP full cells using pristine PP separator show rapid capacity decay after only 60 cycles. In strong contrast, Li//LFP full cells using BN@PP separator exhibit a stable cycling performance of over 170 cycles with a capacity retention of 87.8% and stable voltage profiles. The improved cycling stability could be attributed to BN-based layer on the separator and in situ formed $[LiNBH]_n$-enhanced SEI on Li metal, which could regulate and promote the diffusion of Li ion in both electrolyte and SEI, and guide the uniform plating/stripping of Li.

Li//S cell is considered to be one of the most promising next-generation rechargeable batteries due to the much higher energy density of Li//S cell than Li//LFP and Li//NCM system.[25] Unfortunately, upon cycling at 1 C, Li//S full cell with pristine PP separator shows rapid capacity decay to 364 mA h g^{-1}, corresponding to a capacity retention of merely 34.0% after 300 cycles. The

rapid capacity decay could be attributed to the accumulation of "dead Li" and the thickening of SEI on the surface upon cycling (Figure S47 and S48, Supporting Information), which consumes active Li and increases polarization (Figure S49, Supporting Information). Besides, as evidenced by the higher coulombic efficiency (over 100%) and the stronger signal of S species in element mapping on the surface of cycled Li (Figure S50a and S51, Supporting Information), the severe shuttle effect in Li//S full cell and the serious parasitic reaction between Li and soluble polysulfides in the electrolyte lead to the serious loss of active S and the corrosion of active Li, which is also responsible for the fast capacity degradation upon cycling. By comparison, Li//S full cell using BN@PP separator exhibits a much higher specific capacity of 833 mA h g^{-1}, delivering a capacity retention of 70.2% after 300 cycles with low polarization (Figure 4h; Figure S49, Supporting Information), owing to the dense and uniform deposition/dissolution of Li induced by BN-based layer on the separator and $[LiNBH]_n$-enhanced SEI (Figure S52 and S53, Supporting Information). More importantly, $[LiNBH]_n$-enhanced SEI could also suppress the reaction between polysulfides and Li, which effectively improves the cycling stability of Li//S full cell (Figure S50b and S51, Supporting Information).

3. Conclusion

In conclusion, this work provides a facile strategy to modify commercial PP separator with BN-based layer toward stabilizing Li metal anode. $(NH_2–BH_2)_n$ and $(NH=BH)_n$ species in BN-based layer on PP separator regulate and promote the Li ion diffusion in the electrolyte by weakening the Li bonds between Li ion and solvent, which effectively suppresses the growth of Li dendrites. More importantly, the increase of anion content in the solvation sheath of Li ion and the reaction between Li and $(NH_2–BH_2)_n$ and $(NH=BH)_n$ species are capable of inducing $[LiNBH]_n$-enhanced SEI with higher content of Li_3N and LiF, which is able to promote Li ion diffusion kinetics inside of thus-formed SEI layers. Moreover, the formation of $[LiNBH]_n$ could not only increase the toughness of SEI to tolerate the volume variation during Li stripping/plating, but also guide the uniform deposition of Li due to the homogeneous presence of Li–N and B–N bonds with high polarity. As a result, the cycle life of Li symmetric cells using BN@PP as the separator at 1 mA cm^{-2} with a capacity of 1 mA h cm^{-2} could be extended to over 4000 h. When coupled with commercial LFP ($LiFePO_4$: 12 mg cm^{-2}) as the cathode, the assembled full cells achieve favorable cycling stability of over 500 cycles at 1 C. More interestingly, BN@PP separator could be universally applied in stabilizing Na and K metal anodes. This work may give a spark of inspiration for the design and construction of advanced separator, which could not only regulate ion diffusion in the electrolyte but also promote the construction of stable SEI toward stabilizing alkali metal anode.

4. Experimental Section

Fabrication of BN@PP: Commercial PP separator was first immersed in 0.3 M AB/THF solution for 3 min, which was then dried and heated at 100 °C for 10 min to remove residual THF and enable initial dehydrogenation of AB on PP separator. After repeated immersion and heat treatment for several times, the modified PP separator was finally heated at 100, 120, 140, or 160 °C for 30 min to obtain BN@PP. The mass loading of BN-based layer was calculated according to the following equation: mass loading = $(m_{after}\text{-}m_{before})/S$, where m_{after} and m_{before} were the total weight of PP separator after and before BN-based layer loading, respectively, and S was the surface area of PP separator (Figure S2, Supporting Information).

Materials Characterization: The morphology detection of as-prepared samples was obtained with a field emission scanning electron microscope (FE-SEM; ZEISS Gemini 300). Fourier-transform infrared (FTIR) tests were performed on Thermo Scientific Nicolet iS5. Solid-state nuclear magnetic resonance (solid-state NMR; Bruker AVANCE III 500 MHz) experiments were measured with a solid-state magic angle spinning (MAS) probe. X-ray photoelectron spectroscopy (XPS; Thermo Scientific K-Alpha$^+$) experiments were conducted with single X-ray source, using an Al Kα (1486 eV) anode. All binding energies were calibrated by using the contaminant carbon (C 1s = 284.8 eV) as a reference. The Young's modulus of samples was calculated based on the force curves acquired on an atomic force microscope (AFM; Bruker Dimension Icon) with a contact mode.

Electrochemical Measurement: CR2032 type coin cells with Celgard PP separator were used to assemble all the cells. 1 M LiTFSI in DOL and DME (1:1 in volume) with 1 wt.% $LiNO_3$ was employed as electrolyte of Li symmetric and Li//S cells. 1 M $LiPF_6$ in EC and DEC (1/1 in volume) with the addition of 10 wt.% fluoroethylene carbonate (FEC) and 1% vinylene carbonate (VC) was used as electrolyte of Li symmetric, Li//LFP and Li//NCM523 cells. 1 M sodium hexafluorophosphate ($NaPF_6$) in diglyme was used as electrolyte of Na symmetric cells. 1 M potassium bis(fluorosulfonyl)amide (KFSI) in DME was used as electrolyte of K symmetric cells. The volume of electrolyte in each cell was controlled to be ≈30 µl.

In symmetric cells, bare alkali metal (Li, Na, and K) was used as both working and counter electrodes. LFP and NCM523 cathodes in Li//LFP and Li//NCM523 full cells were purchased from Canrd (Guangdong Canrd New Energy Technology Co., Ltd). The areal mass loading of LFP and NCM523 was ≈12 and 10 mg cm^{-2}, respectively. The mass loading of LFP cathodes with high areal capacity was ≈30 mg cm^{-2}, equaling to an areal capacity of 5.1 mA h cm^{-2}. In Li//S full cells, the carbon-sulfur composite was first prepared by mixing and heating CMK-3 and sublimated sulfur (4:6 in weight) at 155 °C for 12 h. Subsequently, sulfur cathodes were prepared by casting the slurry containing as-prepared carbon-sulfur composite, carbon nanotubes (CNTs), and polyvinylidene fluoride (PVDF) with a mass ratio of 8:1:1 in N-methyl-2-pyrrolidinone (NMP) on Al foil, followed by vacuum-drying at 55 °C for 12 h. The loading amount of S on sulfur cathodes was ≈1.7 mg cm^{-2}. Before assembling cells, all electrodes (e.g., LFP, NCM523 and sulfur cathodes, and Li metal anode) were punched into disks with a diameter of 12 mm. The thickness of Li metal anode in full cell tests was controlled to be ≈100 µm.

The galvanostatic charge/discharge measurements of symmetric cells and full cells were performed on a LAND battery testing system at room temperature. The voltage window was 2.5–4 V, 3–4.3 V, and 1.7–2.8 V for Li//LFP, Li//NCM523, and Li//S full cells, respectively. EIS measurements were performed in the frequency range from 100 kHz to 0.1 kHz. Linear sweep voltammetry (LSV) was conducted in a range between −200 and 200 mV with a sweep rate of 1 mV s^{-1}. The corresponding exchange current density was calculated by fitting Tafel plots from −150 to −100 mV. The ionic conductivity of bare PP and BN@PP was calculated according to the following equation: $\sigma = L/(S{\cdot}R)$, where Li was the thickness of separator, S was the surface area of the electrolyte and stainless steel electrode, R was obtained from the EIS plot of SS//SS cell. To evaluate the Li ion transference number ($t_{Li}{}^+$) of bare PP and BN@PP, Li symmetric cells were first assembled, and then a fixed voltage of 10 mV was applied to the symmetric cells for 1500 s. The Li ion transference number was obtained by $t_{Li}{}^+ = I_s{\cdot}(\Delta V\text{-}I_i{\cdot}R_s)/I_i{\cdot}(\Delta V\text{-}I_s{\cdot}R_i)$, where ΔV was the voltage bias, I_i and I_s stand for initial and steady-state currents, R_i and R_s represent electrochemical resistances of symmetric cells before and after test. All these measurements were performed on a VMP-3 electrochemical workstation (Bio-Logic).

Models and Computational Details: In this work, a standard molecular mechanics potential model was used with the following functional form:

$$u\left(r^N\right) = \sum_{bonds} \frac{k_i}{2}\left(l_i - l_{i,0}\right)^2 + \sum_{angles} \frac{k_i}{2}\left(\theta_i - \theta_{i,0}\right)^2 + \sum_{torsions} \frac{V_n}{2}\left(1 + \cos\left(n\omega - \gamma\right)\right) + \sum_{i=1}^{N}\sum_{j=i+1}^{N}\left(4\varepsilon_{ij}\left[\left(\frac{\sigma_{ij}}{r_{ij}}\right)^{12} - \left(\frac{\sigma_{ij}}{r_{ij}}\right)^{6}\right] + \frac{q_i q_j}{r_{ij}}\right) \quad (3)$$

where the first three terms were the bonded interactions, including bond, angle, and torsion interactions, and the second terms were nonbonded interactions, including van der Waals (vdW) and Coulombic interactions. For different kinds of atoms, the Lorentz-Berthelot mix rules were adopted for vdW interactions, which was following the equation:

$$\sigma_{ij} = \frac{1}{2}\left(\sigma_{ii} + \sigma_{jj}\right); \varepsilon_{ij} = \left(\varepsilon_{ii} * \varepsilon_{jj}\right)^{1/2} \quad (4)$$

According to the experimental conditions, six systems were constructed. The initial configurations of the systems were constructed using the Packmol software.[26] The simulations were performed using GROMACS package (version 2019.3)[27] with the all-atom OPLS (optimized performance for liquid systems) force field..[28] For each system, the steep descent method was used to minimize the energy of the system. Then, molecular dynamics simulations under NPT ensemble at 298 K and 1 atm were performed for 10 ns for each system to collect trajectories for the subsequent data analysis. LINCS algorithm[29] was applied to constrain the bond lengths of other components. Periodic boundary conditions were applied in all three directions. The temperature was maintained using the V-rescale thermostat algorithm.[30] The cut-off distance for the Lennard-Jones and electrostatic interactions was 1.2 nm. Particle mesh Ewald method[31] was used to calculate the long-range electrostatic interactions. Configurations were visualized using Visual Molecular Dynamics software.[32]

DFT Calculations: The models in DFT calculation were selected according to the structures of PP, DME, NH_3BH_3, and the derivatives of NH_3BH_3 in previously reported works.[33] The interaction between NH_3BH_3 and PP was calculated according to the configuration with the lowest energy in NH_3BH_3-PP models, by changing the direction of NH_3BH_3 molecule and adjusting the distance between NH_3BH_3 and PP with the optimization of structure.

The local orbital density functional method was used to study the interaction between PP separator and AB molecules, and the dissociation energy when Li^+ coordinates with two DME molecular without and with the introduction of $(NH_2\text{-}BH_2)_n$ and $(NH = BH)_n$. The generalized gradient approximation (GGA) in Perdew-Burke-Ernzerhof (PBE) functional[34] was used to describe the exchange-correlation potential. The valence orbitals of the atoms were described using the localized double-numerical basis sets with polarization functions (DNP). The real-space cutoff was set to be 4.5 Å.

Supporting Information

Supporting Information is available from the Wiley Online Library or from the author.

Acknowledgements

This work was partially supported by the National Key R&D Program of China (2021YFB3802400), the National Natural Science Foundation of China (22279020, 51971065, U2130208, 52071156, and 51901045), the Science and Technology Commission of Shanghai Municipality (No. 21ZR1407500), and the Innovation Program of Shanghai Municipal Education Commission (2019-01-07-00-07-E00028).

Conflict of Interest

The authors declare no conflict of interest.

Data Availability Statement

The data that support the findings of this study are available in the supplementary material of this article.

Keywords

BN@PP, $[LiNBH]_n$-enhanced SEI, Li dentrites, Li metal anodes, solvation structures

Received: February 20, 2023
Revised: April 17, 2023
Published online: May 18, 2023

[1] a) P. Albertus, S. Babinec, S. Litzelman, A. Newman, *Nat. Energy* **2018**, *3*, 16; b) J. Liu, Z. Bao, Y. Cui, E. J. Dufek, J. B. Goodenough, P. Khalifah, Q. Li, B. Y. Liaw, P. Liu, A. Manthiram, Y. S. Meng, V. R. Subramanian, M. F. Toney, V. V. Viswanathan, M. S. Whittingham, J. Xiao, W. Xu, J. Yang, X. Q. Yang, J. G. Zhang, *Nat. Energy* **2019**, *4*, 180; c) L. Grande, E. Paillard, J. Hassoun, J. B. Park, Y. J. Lee, Y. K. Sun, S. Passerini, B. Scrosati, *Adv. Mater.* **2015**, *27*, 784.

[2] a) Y. Guo, H. Li, T. Zhai, *Adv. Mater.* **2017**, *29*, 1700007; b) P. Zhai, T. Wang, H. Jiang, J. Wan, Y. Wei, L. Wang, W. Liu, Q. Chen, W. Yang, Y. Cui, Y. Gong, *Adv. Mater.* **2021**, *33*, 2006247; c) C. Jin, T. Liu, O. Sheng, M. Li, T. Liu, Y. Yuan, J. Nai, Z. Ju, W. Zhang, Y. Liu, Y. Wang, Z. Lin, J. Lu, X. Tao, *Nat. Energy* **2021**, *6*, 378.

[3] a) X. Zhang, Y. Yang, Z. Zhou, *Chem. Soc. Rev.* **2020**, *49*, 3040;. b) Y. Ma, L. Wei, Y. He, X. Yuan, Y. Su, Y. Gu, X. Li, X. Zhao, Y. Qin, Q. Mu, Y. Peng, Y. Sun, Z. Deng, *Angew. Chem., Int. Ed.* **2022**, *61*, e202116291.

[4] a) X. B. Cheng, R. Zhang, C. Z. Zhao, Q. Zhang, *Chem. Rev.* **2017**, *117*, 10403;. b) Y. Xu, L. Gao, L. Shen, Q. Liu, Y. Zhu, Q. Liu, L. Li, X. Kong, Y. Lu, H. B. Wu, *Matter* **2020**, *3*, 1685.

[5] a) D. Lin, Y. Liu, Y. Cui, *Nat. Nanotechnol.* **2017**, *12*, 194;. b) H. Huo, X. Li, Y. Chen, J. Liang, S. Deng, X. Gao, K. Doyle-Davis, R. Li, X. Guo, Y. Shen, C. W. Nan, X. Sun, *Energy Storage Mater.* **2020**, *29*, 361; c) Z. Peng, N. Zhao, Z. Zhang, H. Wan, H. Lin, M. Liu, C. Shen, H. He, X. Guo, J. G. Zhang, D. Wang, *Nano Energy* **2017**, *39*, 662.

[6] H. Zhang, S. Ju, G. Xia, D. Sun, X. Yu, *Adv. Funct. Mater.* **2021**, *31*, 2009712.

[7] B. Liu, J. G. Zhang, W. Xu, *Joule* **2018**, *2*, 833.

[8] a) Q. Zhao, Z. Tu, S. Wei, K. Zhang, S. Choudhury, X. Liu, L. A. Archer, *Angew. Chem., Int. Ed.* **2018**, *57*, 992; b) X. Ren, Y. Zhang, M. H. Engelhard, Q. Li, J. G. Zhang, W. Xu, *ACS Energy Lett.* **2018**, *3*, 14; c) Z. Wang, F. Qi, L. Yin, Y. Shi, C. Sun, B. An, H. M. Cheng, F. Li, *Adv. Energy Mater.* **2020**, *10*, 1903843; d) F. Ding, W. Xu, G. L. Graff, J. Zhang, M. L. Sushko, X. Chen, Y. Shao, M. H. Engelhard, Z. Nie, J. Xiao, X. Liu, P. V. Sushko, J. Liu, J. G. Zhang, *J. Am. Chem. Soc.* **2013**, *135*, 4450.

[9] a) F. Liu, L. Wang, Z. Zhang, P. Shi, Y. Feng, Y. Yao, S. Ye, H. Wang, X. Wu, Y. Yu, *Adv. Funct. Mater.* **2020**, 30; b) N. W. Li, Y. Shi, Y. X. Yin, X. X. Zeng, J. Y. Li, C. J. Li, L. J. Wan, R. Wen, Y. G. Guo, *Angew. Chem., Int. Ed.* **2018**, *57*, 1505; c) W. Tang, X. Yin, S. Kang, Z. Chen, B. Tian, S. L. Teo, X. Wang, X. Chi, K. P. Loh, H. W. Lee, G. W. Zheng, *Adv. Mater.* **2018**, *30*, 1801745; d) R. Pathak, K. Chen, A. Gurung, K. M. Reza, B. Bahrami, J. Pokharel, A. Baniya, W. He, F. Wu, Y. Zhou, K. Xu, Q. Qiao, *Nat. Commun.* **2020**, *11*, 93.

[10] a) Z. Y. Wang, Z. X. Lu, W. Guo, Q. Luo, Y. H. Yin, X. B. Liu, Y. S. Li, B. Y. Xia, Z. P. Wu, *Adv. Mater.* **2021**, *33*, 2006702; b) X. Y. Yue, Q. Y.

Zhou, J. Bao, C. Ma, S. Y. Yang, X. L. Li, D. Sun, F. Fang, X. J. Wu, Y. N. Zhou, *Adv. Funct. Mater.* **2021**, *31*, 2008786; c) H. Wang, D. Lin, Y. Liu, Y. Li, Y. Cui, *Sci Adv* **2017**, *3*, e1701301; d) T. Zhang, H. Lu, J. Yang, Z. Xu, J. Wang, S. Hirano, Y. Guo, C. Liang, *ACS Nano* **2020**, *14*, 5618; e) S. S. Chi, Y. Liu, W. L. Song, L. Z. Fan, Q. Zhang, *Adv. Funct. Mater.* **2017**, *27*, 1700348; f) Y. Cheng, X. Ke, Y. Chen, X. Huang, Z. Shi, Z. Guo, *Nano Energy* **2019**, *63*, 103854.

[11] C. Z. Zhao, P. Y. Chen, R. Zhang, X. Chen, B. Q. Li, X. Q. Zhang, X. B. Cheng, Q. Zhang, *Sci. Adv.* **2018**, *4*, eaat3446.

[12] a) Y. Liu, S. Xiong, J. Wang, X. Jiao, S. Li, C. Zhang, Z. Song, J. Song, *Energy Storage Mater.* **2019**, *19*, 24; b) X. Chen, R. Zhang, R. Zhao, X. Qi, K. Li, Q. Sun, M. Ma, L. Qie, Y. Huang, *Energy Storage Mater.* **2020**, *31*, 181; c) C. Li, S. Liu, C. Shi, G. Liang, Z. Lu, R. Fu, D. Wu, *Nat. Commun.* **2019**, *10*, 1363;. d) Y. Yang, S. Yao, Z. Liang, Y. Wen, Z. Liu, Y. Wu, J. Liu, M. Zhu, *ACS Energy Lett.* **2022**, *7*, 885.

[13] W. Ren, Y. Zheng, Z. Cui, Y. Tao, B. Li, W. Wang, *Energy Storage Mater.* **2021**, *35*, 157.

[14] a) T. Kobayashi, S. Gupta, M. A. Caporini, V. K. Pecharsky, M. Pruski, *J. Phys. Chem. C* **2014**, *118*, 19548; b) R. P. Shrestha, H. V. K. Diyabalanage, T. A. Semelsberger, K. C. Ott, A. K. Burrell, *Int. J. Hydrogen Energy* **2009**, *34*, 2616.

[15] B. Roy, U. Pal, A. Bishnoi, L. A. O'Dell, P. Sharma, *Chem. Commun.* **2021**, *57*, 1887.

[16] a) S. Frueh, R. Kellett, C. Mallery, T. Molter, W. S. Willis, C. King'ondu, S. L. Suib, *Inorg. Chem.* **2011**, *50*, 783;. b) Z. Wang, Y. Wang, Z. Zhang, X. Chen, W. Lie, Y. B. He, Z. Zhou, G. Xia, Z. Guo, *Adv. Funct. Mater.* **2020**, *30*, 2002414.

[17] A. Al-Kukhun, H. T. Hwang, A. Varma, *Int. J. Hydrogen Energy* **2013**, *38*, 169.

[18] a) X. Chen, Y. K. Bai, C. Z. Zhao, X. Shen, Q. Zhang, *Angew. Chem., Int. Ed.* **2020**, *59*, 11192; b) X. Chen, Q. Zhang, *Acc. Chem. Res.* **2020**, *53*, 1992;. c) S. Feng, Z. H. Fu, X. Chen, Q. Zhang, *InfoMat* **2022**, *4*, e12304; d) T. Z. Hou, W. T. Xu, X. Chen, H. J. Peng, J. Q. Huang, Q. Zhang, *Angew. Chem., Int. Ed.* **2017**, *56*, 8178.

[19] a) D. Wu, J. He, J. Liu, M. Wu, S. Qi, H. Wang, J. Huang, F. Li, D. Tang, J. Ma, *Adv. Energy Mater* **2022**, *12*, 2200337; b) Z. Shadike, H. Lee, O. Borodin, X. Cao, X. Fan, X. Wang, R. Lin, S. M. Bak, S. Ghose, K. Xu, C. Wang, J. Liu, J. Xiao, X. Q. Yang, E. Hu, *Nat. Nanotechnol.* **2021**, *16*, 549.

[20] a) X. Fan, X. Ji, L. Chen, J. Chen, T. Deng, F. Han, J. Yue, N. Piao, R. Wang, X. Zhou, X. Xiao, L. Chen, C. Wang, *Nat. Energy* **2019**, *4*, 882; b) X. Fan, X. Ji, F. Han, J. Yue, J. Chen, L. Chen, T. Deng, J. Jiang, C. Wang, *Sci. Adv.* **2018**, *4*, eaau9245;. c) J. Xie, L. Liao, Y. Gong, Y. Li, F. Shi, A. Pei, J. Sun, R. Zhang, B. Kong, R. Subbaraman, J. Christensen, Y. Cui, *Sci Adv* **2017**, *3*, eaao3170; d) C. Cui, C. Yang, N. Eidson, J. Chen, F. Han, L. Chen, C. Luo, P. F. Wang, X. Fan, C. Wang, *Adv. Mater.* **2020**, *32*, 1906427; e) Y. Jie, X. Ren, R. Cao, W. Cai, S. Jiao, *Adv. Funct. Mater.* **2020**, *30*, 1910777.

[21] a) X. R. Chen, Y. X. Yao, C. Yan, R. Zhang, X. B. Cheng, Q. Zhang, *Angew. Chem., Int. Ed.* **2020**, *59*, 7743; b) Y. Luo, T. Li, H. Zhang, W. Liu, X. Zhang, J. Yan, H. Zhang, X. Li, *Angew. Chem., Int. Ed.* **2021**, *60*, 11718.

[22] a) S. Ni, M. Zhang, C. Li, R. Gao, J. Sheng, X. Wu, G. Zhou, *Adv. Mater.* **2023**, *35*, 2209028; b) M. S. Kim, Z. Zhang, J. Wang, S. T. Oyakhire, S. C. Kim, Z. Yu, Y. Chen, D. T. Boyle, Y. Ye, Z. Huang, W. Zhang, R. Xu, P. Sayavong, S. F. Bent, J. Qin, Z. Bao, Y. Cui, *ACS Nano* **2023**, *17*, 3168.

[23] a) K. Park, J. B. Goodenough, *Adv. Energy Mater.* **2017**, *7*, 1700732; b) S. Liu, X. Ji, N. Piao, J. Chen, N. Eidson, J. Xu, P. Wang, L. Chen, J. Zhang, T. Deng, S. Hou, T. Jin, H. Wan, J. Li, J. Tu, C. Wang, *Angew. Chem., Int. Ed.* **2021**, *60*, 3661; c) Y. Liu, X. Tao, Y. Wang, C. Jiang, C. Ma, O. Sheng, G. Lu, X. W. Lou, *Science* **2022**, *375*, 739.

[24] C. Wei, Y. Tao, H. Fei, Y. An, Y. Tian, J. Feng, Y. Qian, *Energy Storage Mater.* **2020**, *30*, 206.

[25] E. Cha, M. D. Patel, J. Park, J. Hwang, V. Prasad, K. Cho, W. Choi, *Nat. Nanotechnol.* **2018**, *13*, 337.

[26] L. Martínez, R. Andrade, E. G. Birgin, J. M. Martínez, *J. Comput. Chem.* **2009**, *30*, 2157.

[27] a) M. J. Abraham, T. Murtola, R. Schulz, S. Páll, J. C. Smith, B. Hess, E. Lindahl, *SoftwareX* **2015**, *1–2*, 19; b) S. Pronk, S. Páll, R. Schulz, P. Larsson, P. Bjelkmar, R. Apostolov, M. R. Shirts, J. C. Smith, P. M. Kasson, D. van der Spoel, B. Hess, E. Lindahl, *Bioinformatics* **2013**, *29*, 845;. c) B. Hess, C. Kutzner, D. van der Spoel, E. Lindahl, *J. Chem. Theory Comput.* **2008**, *4*, 435.

[28] W. L. Jorgensen, D. S. Maxwell, J. Tirado-Rives, *J. Am. Chem. Soc.* **1996**, *118*, 11225.

[29] B. Hess, H. Bekker, H. J. C. Berendsen, J. G. E. M. Fraaije, *J. Comput. Chem.* **1997**, *18*, 1463.

[30] G. Bussi, D. Donadio, M. Parrinello, *J. Chem. Phys.* **2007**, *126*, 014101.

[31] U. Essmann, L. Perera, M. L. Berkowitz, T. Darden, H. Lee, L. G. Pedersen, *J. Chem. Phys.* **1995**, *103*, 8577.

[32] W. Humphrey, A. Dalke, K. Schulten, *J Mol Graph* **1996**, *14*, 33.

[33] a) P. M. Zimmerman, A. Paul, Z. Zhang, C. B. Musgrave, *Inorg. Chem.* **2009**, *48*, 1069;. b) J. W. Mullinax, C. W. Bauschlicher Jr., J. W. Lawson, *J. Phys. Chem. A* **2022**, *126*, 7997;. c) M. G. El-Desouky, M. Abd El-Wahab, A. A. El-Bindary, *Biointerface Res. Appl. Chem.* **2022**, *12*, 1134.

[34] a) J. P. Perdew, K. Burke, M. Ernzerhof, *Phys. Rev. Lett.* **1996**, *77*, 3865;. b) J. P. Perdew, K. Burke, Y. Wang, *Phys. Rev. B* **1996**, *54*, 16533.